Modular assembly of metal nanoparticles/ mesoporous carbon two-dimensional nanosheets

Pengpeng Qiu[1,2], Xingmiao Zhang[1], Yan Ai[1], Wei Luo[2], Wei Li[1] and Dongyuan Zhao[1]

Abstract

The manipulation of polymeric micelles across extended-length scales is a key challenge in the design of integrated mesoporous materials with well-defined geometry and advanced functions. Herein, we demonstrate a modular assembly strategy to construct metal nanoparticle functionalized mesoporous carbon two-dimensional (2D) nanosheets by organizing zero-dimensional (0D) spherical monomicelle modules on the 2D supporting blocks. The modular assembly process involves two key steps: the "modularization" step is used to synthesize highly uniform metal–catecholamine (MC) complex functionalized monomicelle "modules" that can be conveniently assembled on the 2D supporting blocks (graphene oxide (GO), WS_2, and MXene) in the following "assembly" step. After an annealing process, the resultant composites possess a single-layered 2D nanosheet surrounded by two single-layered mesoporous carbon at both sides and exhibit highly ordered mesostructures with large surface areas ($\sim$385 m^2 g^{-1}), tunable pore sizes (16–25 nm) and highly dispersed metal-containing nanoparticles. Due to the modularity of this assembly process, a range of metal species (Co, Fe, Ni, V, Cu, Pd, FeCo, CoNi, and FeCoNi) can be in-situ incorporated into the 2D mesoporous frameworks, which are partially embedded in the pore walls with the remaining part exposed in the pore channels. Benefiting from the unique textual structures, the resultant GO-derived functional mesoporous carbon nanosheets (Co as the functional species and being annealed at 850 °C) exhibit excellent electrocatalytic activity, long-term stability, and superior methanol tolerance for oxygen reduction reaction, which holds great potential as a catalyst for fuel cells.

Introduction

Nature is abundant in self-assembled objects with fascinating properties such as tough nacre, superhydrophobic lotus leaves, and photonic butterfly wings[1–3]. Inspired by these assemblies, tremendous efforts have been devoted to construct advanced materials with complex nanostructures by artificial self-assembly from a toolkit of chemical building blocks, such as micelles, vesicles, films, and tubes[4–6]. As a typical product from the assembly of polymeric micelles, ordered mesoporous materials (OMMs) have experienced great development over the past three decades, producing a series of OMMs with unique mesostructures, various compositions, and diverse architectures[7–11]. Particularly, the construction of two-dimensional (2D) mesoporous materials (2DMMs) has recently provided increasing opportunities for the fabrication of novel electronic materials, superior energy conversion and storage devices, and excellent catalysts due to the integrated properties from the ultrathin 2D nanosheet structure and ordered mesoporous frameworks[12–14]. In addition, the applicability of 2DMMs could be tremendously enhanced if some functional metal nanoparticles (NPs) with different features could be in-situ confined inside the mesopores to create materials with desired properties[15–17]. However, metal ions are highly electrophilic and can easily react with the nucleophiles like water, thus it is difficult to obtain homogenous organic–inorganic mesoporous preforms through the

Correspondence: Wei Luo (wluo@dhu.edu.cn) or
Wei Li (weilichem@fudan.edu.cn)
[1]Department of Chemistry, Laboratory of Advanced Materials, Shanghai Key Laboratory of Molecular Catalysis and Innovative Materials, iChEM and State Key Laboratory of Molecular Engineering of Polymers, Fudan University, 200433 Shanghai, China
[2]State Key Laboratory for Modification of Chemical Fibers and Polymer Materials, College of Materials Science and Engineering, Donghua University, 201620 Shanghai, China

conventional wet-chemistry approach. In addition, the lack of suitable molecular interactions between the metal atoms and framework precursors leads to the uncontrolled growth of metal species during the calcination, which may result in the migration of NPs into the mesopores, blocking the electron/ion transport channels of the mesoporous frameworks. Therefore, a generalized bottom-up strategy for controlled in-situ incorporation of functional metal NPs in a 2D mesoporous nanostructure at a molecular self-assembly level is greatly desired but remains a great challenge.
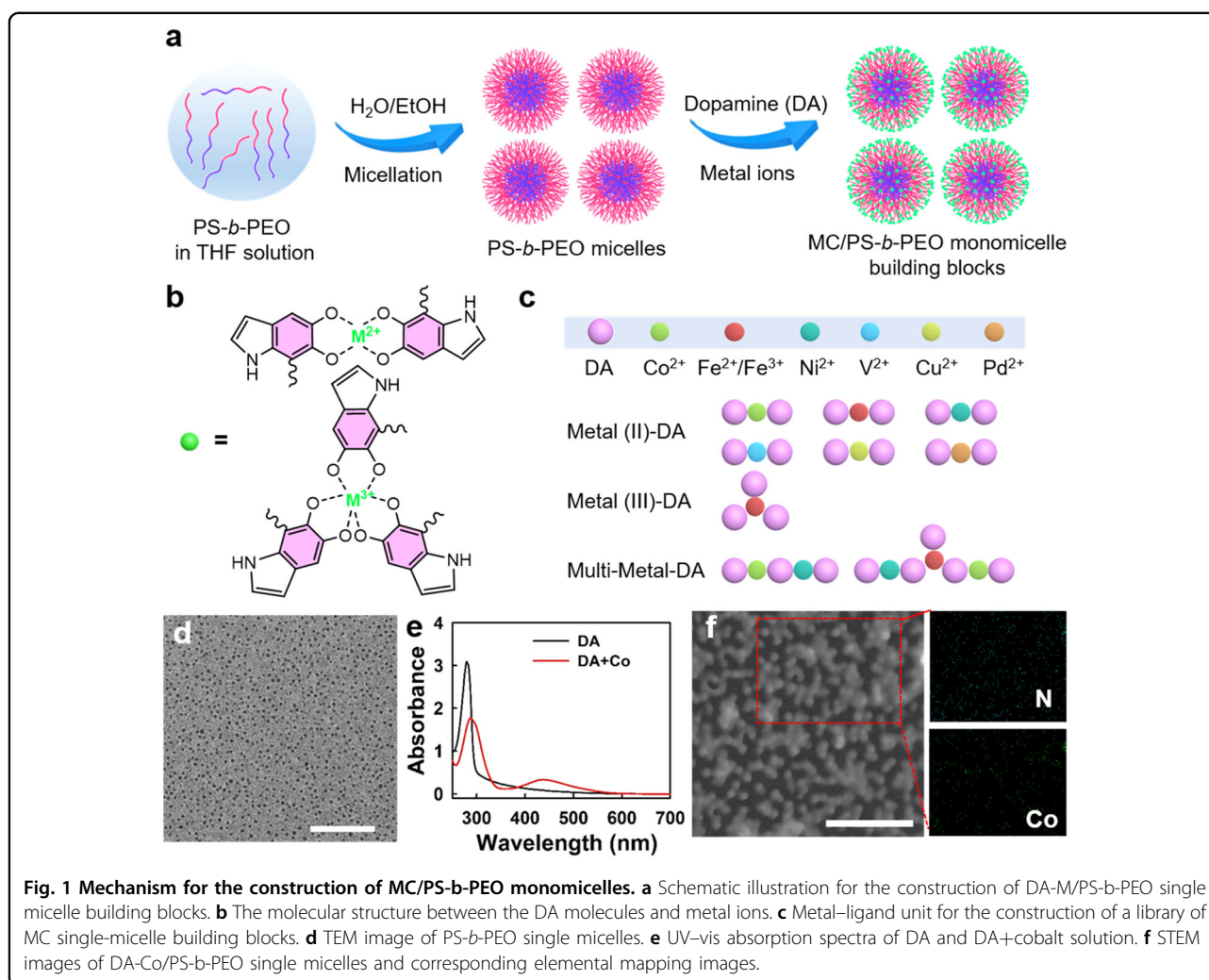
Recently, the metal–ligand-assisted self-assembly has been exploited as a powerful bottom-up approach to construct various metal-organic complexes on some NPs that could be further applied as the modular "building blocks" for constructing higher-order superstructures with increased complexity and functionality[18–20]. Considering the modularity of coordination-driven assembly, the surface properties of a given supramolecular monomicelle core can also be readily modularized and thus have a significant effect on the resulting mesoporous materials. More importantly, the formation of metal–ligand bonds may work in parallel with noncovalent interactions (e.g. electrostatic attraction, hydrogen bonding, and hydrophobic interaction), which makes it possible to design materials that mimic the hierarchical ordering found in the natural system.

Herein, we report a modular assembly strategy to construct metallic NPs functionalized mesoporous carbon sandwich nanosheets from the metal–catecholamine (MC) monomicelle building blocks. This strategy involves two key steps: (i) metal–catecholamine functionalization of readily formed polystyrene-block-polyethylene oxide (PS-b-PEO) monomicelles to construct a library of spherical MC modules; (ii) mounting the modules on the 2D supporting blocks directed by the interfacial molecular interactions and inter-micelles crosslinking using metal ions. Owing to the strong chelation effect of catecholamine groups, a range of single-metal (Co^{2+}, Fe^{2+}, Fe^{3+}, Ni^{2+}, V^{2+}, Cu^{2+}, Pd^{2+}), bi-metal (Fe^{3+}/Co^{2+}, Co^{2+}/Ni^{2+}) and tri-metal ($Fe^{3+}/Co^{2+}/Ni^{2+}$) species can be successfully incorporated into the polymeric frameworks, and then in-situ transformed to metallic NPs followed by an annealing process under inert atmosphere. The resultant materials not only possess well-defined sandwich-like structures with controllable pore sizes (16–25 nm), ultrathin thicknesses (30–50 nm), and high surface areas ($\sim$385 $m^2 g^{-1}$) but also exhibit uniform metal-containing NPs that are homogeneously anchored in the pore walls of the single-layered mesoporous carbon framework. Owing to the unique structure and integrated functionalities, the cobalt NPs incorporated 2D mesoporous carbon catalyst exhibits a high oxygen reduction reaction (ORR) half-wave potential of $\sim$0.82 V, which is comparable to the commercial platinum/carbon (Pt/C) catalyst. Moreover, the catalyst shows high stability and durability under an ultrahigh concentration of menthol (2 $mol\,L^{-1}$). This study paves a promising way to controllably construct functional 2D mesoporous carbon nanosheets for electrochemical applications.

Construction of the library of MC monomicelle modules

The library of MC monomicelle modules was constructed through the metal–catecholamine functionalization of readily formed PS-b-PEO monomicelles (Fig. 1a–c). The diblock copolymer PS-b-PEO templates with various PS lengths were first synthesized through an atom transfer radical polymerization method, which possessed a high quality (Fig. S1). The pure PS-b-PEO block copolymer monomicelles were then formed through the addition of a water/ethanol (2:1) mixture to the PS-b-PEO tetrahydrofuran (THF) solution to form a light-blue colloid solution, which exhibits a clear Tyndall phenomenon (Fig. S2). The formation of such a colloidal solution can be explained as follows: THF is a good solvent for both the PEO and PS chains while water is a good solvent for PEO chains but a poor solvent for the PS chains[21–23]. Therefore, the addition of water significantly increases the repulsion force among the copolymers and thus induces their spontaneous micellization to reduce interface energy. By taking the PS_{222}-b-PEO_{114} copolymer as an example, the transmission electron microscopy (TEM) image (Fig. 1d) clearly shows the formation of uniform spherical micelles with a particle size of $\sim$20 nm. The size is slightly smaller than that measured by a dynamic light scattering ($\sim$22 nm, Fig. S3), possibly owing to the shallow contrast of PEO shells under TEM observation. Finally, the formation of MC/PS-b-PEO monomicelle building blocks was achieved through the metal–catecholamine complex functionalization (Fig. 1a). Here, the dopamine (DA) was used as the carbon precursor because they possess abundant catechol and amine groups that can effectively bind with most inorganic and organic species. Thus, the introduction of DA and metal salts (e.g. $Co(NO_3)_2$) simultaneously into the above solution leads to the formation of MC complexes (Fig. 1b, c), which can be deposited on the PS-b-PEO monomicelles to form the MC/PS-b-PEO composite monomicelles through the hydrogen bonding or electrostatic interaction. The formation of MC complexes was confirmed by measuring the UV–visible spectra of the DA–cobalt mixture solution (Fig. 1e), which shows two clear peaks at the wavelength of 295 and 445 nm, typical for the L_a–L_b transition of DA and the ligand-to-metal charge transfer, respectively[24]. Owing to the high glass temperature of PS blocks, the monomicelles possess very high stability, which acts like colloid nanoparticles. Therefore, the composite single micelles can be separated

Fig. 1 Mechanism for the construction of MC/PS-b-PEO monomicelles. a Schematic illustration for the construction of DA-M/PS-b-PEO single micelle building blocks. **b** The molecular structure between the DA molecules and metal ions. **c** Metal–ligand unit for the construction of a library of MC single-micelle building blocks. **d** TEM image of PS-b-PEO single micelles. **e** UV–vis absorption spectra of DA and DA+cobalt solution. **f** STEM images of DA-Co/PS-b-PEO single micelles and corresponding elemental mapping images.
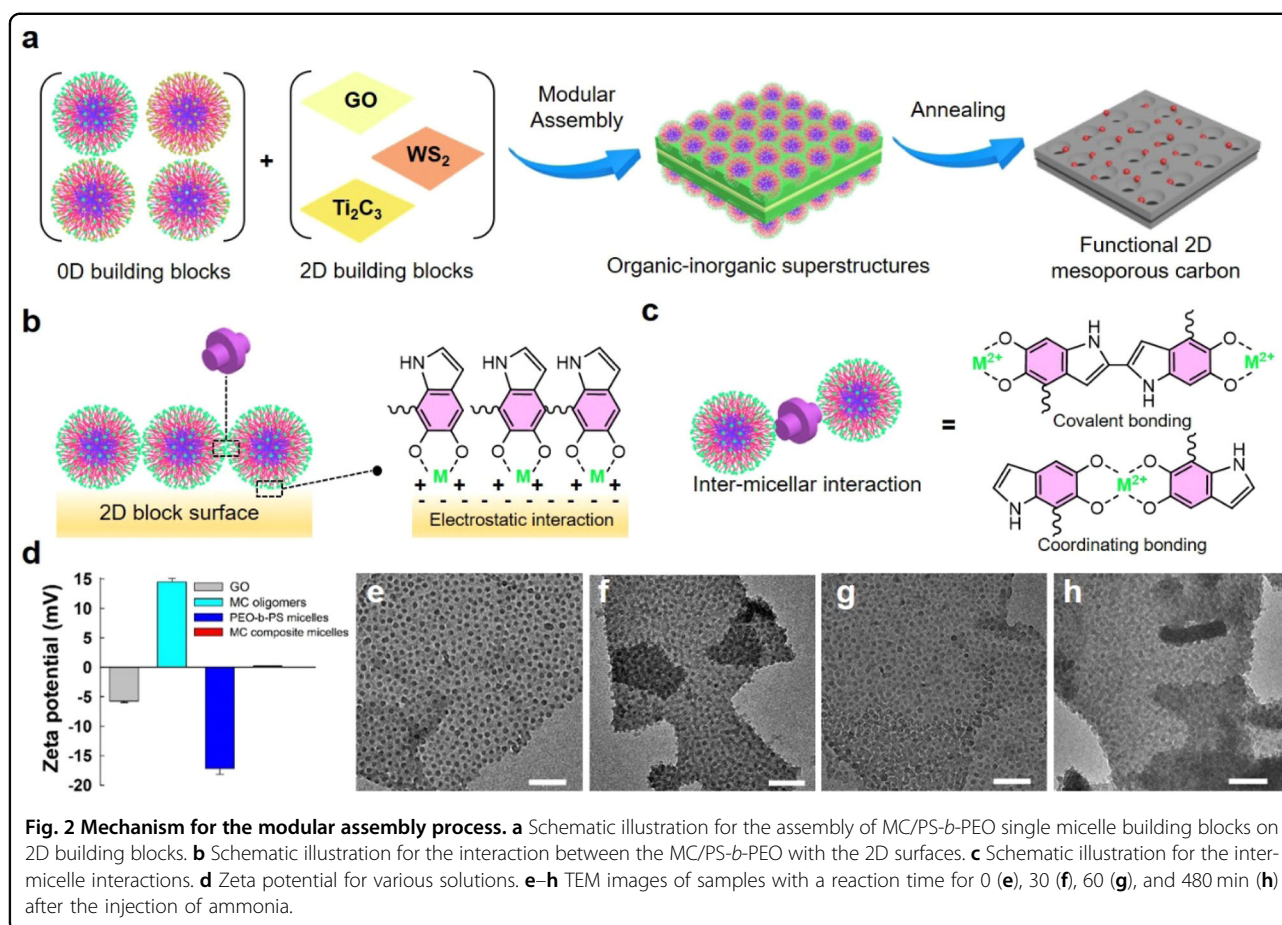
with ultracentrifugation (Fig. S4). The scanning TEM (STEM) image of the collected composite micelles clearly displays that the spherical structure is well-retained and their corresponding energy-dispersive X-ray spectroscopy (EDX) elemental mapping analyses reveal the presence of nitrogen and cobalt elements (Fig. 1f), further confirming the formation of MC/PS-b-PEO monomicelles.

Assembly of MC monomicelle modules on 2D supporting blocks

When the 2D building blocks were added, the pre-formed spherical composite micelles are assembled and anchored on the 2D surfaces (Fig. 2a). TEM images clearly show that the spherical micelles with a diameter of ~20 nm were organized into single-layered architecture with close packing structure on the GO surface (Fig. S5). The driving force for the assembly is proposed to be the electrostatic force between the PEO blocks with the oxygen-bearing groups on GO (such as –COOH and –OH)[25]. Note that an ultrasonic treatment is essential for the further dispersion of GO to maintain its 2D structure (Fig. 2b, d) because the massive opposite-charged solution could lead to the curling of the GO to form a nanowire structure (Fig. S6). The slight adjustment of the solution pH to 8 by the addition of ammonium hydroxide can initiate the polymerization of DA molecules (Fig. 2c). Once the polymerization occurs, the newly formed polymeric dopamine (PDA) oligomers preferentially diffuse and grow around the single micelles on the surface of GO sheets to form a cross-linked network, afterward, resulting in a uniform coating layer on GO sheets to reduce the interfacial energies. Both the TEM and SEM images of the sample withdrawn at different reaction times reveal that the void spaces between the adjacent micelles are gradually filled out by PDA networks (Figs. 2e–h and S7). With extending the reaction for 8 h, the spherical micellar structure on the GO sheets becomes almost invisible and the thickness of the sheet apparently increases (Fig. S7a–c). The EDX mapping spectra show that the elements of carbon, oxygen,

Fig. 2 Mechanism for the modular assembly process. a Schematic illustration for the assembly of MC/PS-*b*-PEO single micelle building blocks on 2D building blocks. **b** Schematic illustration for the interaction between the MC/PS-*b*-PEO with the 2D surfaces. **c** Schematic illustration for the inter-micelle interactions. **d** Zeta potential for various solutions. **e–h** TEM images of samples with a reaction time for 0 (**e**), 30 (**f**), 60 (**g**), and 480 min (**h**) after the injection of ammonia.

nitrogen, and cobalt are uniformly distributed on the whole sheets.

Characterization of the 2D functional mesoporous carbon nanosheets

After the removal of the template, carbonization of the polymeric framework, and crystallization of the metal species, the 2D functional mesoporous carbon nanosheets with tunable pore sizes, various metal species, and different graphitization degrees are obtained and the resultant nanosheets are defined as x@mC-metal-*y* (*x* indicates the type of 2D surface; the metals can be Co, Fe, Ni, Cu, V, and Pd; *y* represents the calcination temperature). Here, we take reduced graphene oxide (rGO) and cobalt as examples of 2D surface and metal species, respectively, for the proof of concept. The SEM images of rGO@mC-Co-550 (Fig. 3a–c) reveal that the functional nanosheets retain the ultrathin 2D layered-nanosheet structure with a thickness of ~36 nm and possess uniform spherical mesopores with a diameter of ~18 nm in large domains. The thickness of the nanosheets is 2 times equal to the pore diameters, suggesting that two layers of mesoporous structure are formed. The partial overlapping of mesopores observed from TEM images (Fig. 3d, e) further

confirms that the mesopores lie on both sides of the rGO, in consistent with SEM side view on the rGO@mC-Co-550 nanosheets (Fig. 3c). These results indicates that the growth of functional carbon nanosheets was directed by the adaptation of the GO sheet morphology into a sandwich-like structure. TEM images also show that uniform functional NPs with a particle size of ~6 nm are evenly dispersed on the entire mesoporous nanosheet frameworks. High-resolution TEM (HRTEM) image further reveals that the CoO nanoparticles with a *d*-spacing of ~0.35 nm that can be assigned to the lattice fringes of CoO (220) are partially embedded in the pore walls with the remaining part exposed in the mesopore channels (Fig. 3f)[26]. It is speculated that this unique semi-exposure structure may not only provide an excellent confinement effect and exposed surface for reactions but also help to tightly trap the nanoparticles and prevent aggregating during the synthesis and applications[27]. Owing to the protection effect, the content of CoO nanoparticles throughout the entire mesoporous framework can be easily tuned by changing the added cobalt nitrate to DA ratio during the synthesis. The TEM images clearly show that as the ratio rises, the distributing density of CoO nanoparticles on the mesoporous nanosheet apparently
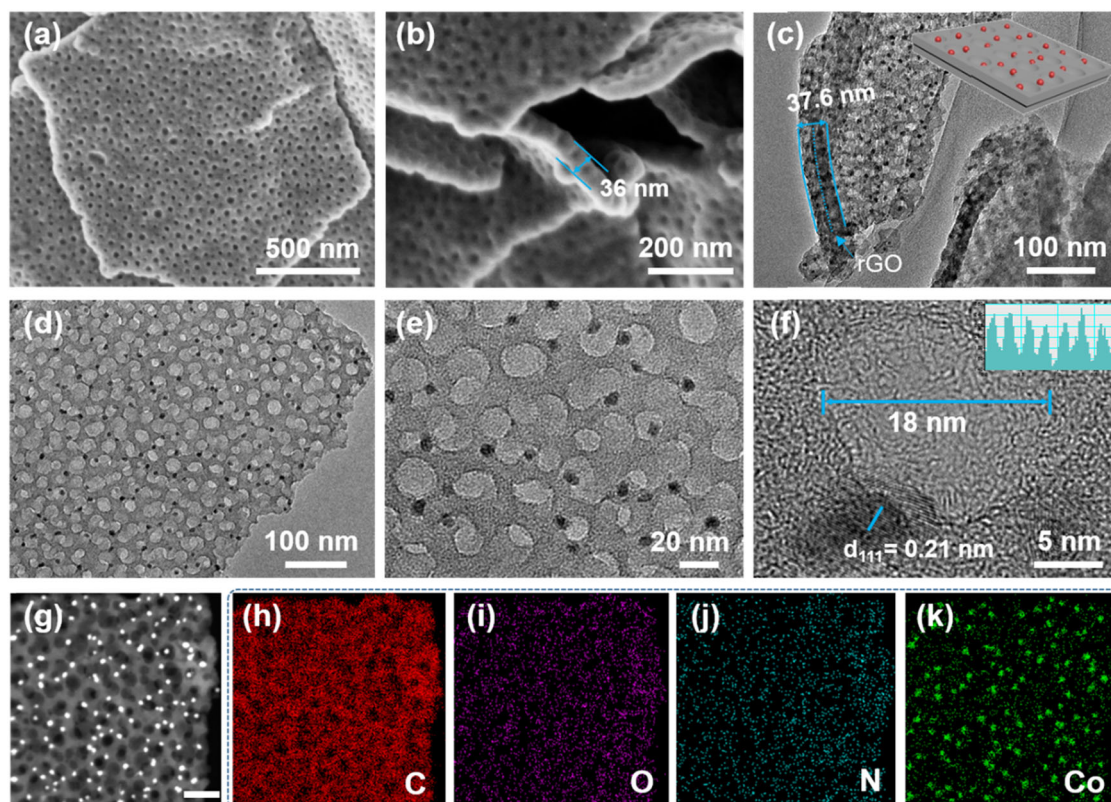
Fig. 3 Structure charaterization of 2D mesoporous rGO@mC-Co-550 nanosheets. a, b SEM, **c–e** TEM, **f** HRTEM and **g** STEM images of the 2D mesoporous rGO@mC-Co-550 nanosheets prepared by using PS_{222}-*b*-PEO_{114} as the template, inset in (**c**) is the model structure of rGO@mC-Co-550; **h–k** EDS elemental mapping spectra of C, O, N, and Co.

increases while the regularity of the mesoporous framework and dispersity of the functional nanoparticles are still well-kept (Fig. S8). The STEM image further confirms that the rGO@mC-Co-550 nanosheets possess a sandwich-like structure with one single rGO layer surrounded by two single-layered mesoporous carbon and many bright dots are evenly distributed in the framework (Fig. 3g). The existence of CoO nanoparticles in the mesoporous framework is evidenced by the EDX elemental mapping of Co and O (Fig. 3h–k). The elemental maps of C and N correspond to the N-doped carbon matrix of 2D nanosheets that forms due to the pyrolysis of amine groups in PDA.

Interestingly, by simply changing the template with a different PS block length, the construction of metal-containing rGO@mC nanosheets with different pore sizes can be achieved. When the PS_{199}-b-PEO_{114} copolymers with a shorter PS block length are used as the template, the pore size decreases to ~15 nm (Fig. S9a, b) while when the template with a longer PS block length is used, the pore size can be extended to ~24 nm (Fig. S9c, d). To get more information on the pore size, the N_2 sorption isotherms of resultant nanosheets were also measured (Fig.

S10), showing a type IV curve with an H_2-type hysteresis loop. The BET surface area is calculated to be 394.7, 385.4, and 365.4 $m^2 g^{-1}$ for the 2D rGO@mC-Co nanosheets prepared with the template of PS_{199}-b-PEO_{114}, PS_{222}-b-PEO_{114}, and PS_{250}-b-PEO_{114}, respectively. Their corresponding pore sizes derived from the adsorption data using the BJH model are 15, 18, and 24 nm, respectively, in consistent with the TEM observation.

The phase purity of the annealed nanosheets at 550 °C is examined by the powder X-ray diffraction (XRD) analysis (Fig. S11), where two typical peaks can be observed. The broadened diffraction peaks at 25.3° can be indexed to graphite while the sharp one at 42.5° is typical for CoO (220). According to the Scherrer formula, the average crystallite size is calculated to be ~6 nm, matching well with the HRTEM result. By arising the calcination temperature, the phase and particle size of the functional nanoparticles could be changed but the ordered mesoporous framework is still maintained (Fig. S12). For further analyzing the surface chemical states of the rGO@mC-Co-550 nanosheets, the X-ray photoelectron spectroscopy (XPS) analysis was performed. The total

survey spectrum (Fig. S13) clearly shows the presence of C, O, N, and Co elements in the nanosheets compared with C and O in the GO, suggesting the formation of N and Co-containing carbon materials. The N 1s XPS spectrum of rGO@mC-Co-550 (Fig. S14) can be deconvoluted into three peaks, which are attributed to pyridinic-N (398.9 eV), pyrrolic-N (400.8 eV) and graphitic-N (402.6 eV), respectively[28]. Nitrogen is a relatively high electronegative heteroatom that could create charged sites for carbon frameworks to improve the electrocatalytic properties of carbon material. Moreover, pyridinic-N and pyrrolic-N are the dominant species, which is more favorable for the ORR (Table S2)[29,30]. As for the Co element, two peaks at 782.0 and 770 eV could be observed, which are in consistent with Co 2p1/2 and Co 2p3/2 binding energy of CoO, respectively. The high-resolution XPS spectra of O1s (Fig. S15) also shows the presence of a Co–O peak, further indicating the formation of CoO species in the 2D nanosheet, which is in good agreement with the HRTEM results. The Raman spectrum of the resultant samples was also recorded to investigate the degree of graphitization (Fig. S16). The peaks at 1340 and 1588 cm^{-1} correspond to the sp^3 disordered carbon (D band) and sp^2 graphitic carbon (G band), respectively. The peak intensity ratio of D to G bands (I_D/I_G) decreases after rising the calcination temperature, suggesting an enhanced degree of graphitization.

Extension of modular assembly to other metals and 2D building blocks

It is worth noting that this modular assembly strategy can be facilely extended to synthesize other metal species containing 2D mesoporous carbon nanosheets such as Fe, Ni, V, Cu, and Pd. The TEM images clearly show that ordered 2D mesoporous rGO@mC-Fe-550, rGO@mC-Ni-550, rGO@mC-V-550, rGO@mC-Cu-550, and rGO@mC-Pd-550 nanosheet can be obtained with uniform spherical mesopores and evenly distributed nanoparticles (Fig. 4a–e). Owing to the difference in the property of metals, the size and crystallinity of the resultant nanoparticles could be different but all are well embedded in the mesoporous frameworks under the protection of carbon wall. In addition, dual and tri-metals containing nanoparticles can also be incorporated into the 2D mesoporous carbon frameworks. Both the TEM and STEM images suggested that well-dispersed nanoparticles with uniform size were embedded in the mesoporous framework (Figs. 4f–h and S17a). The corresponding EDS mapping analysis also shows that the distribution of multi-metals overlapped, indicating the formation of alloy nanoparticles (Figs. 4h and S17b–f). More importantly, by changing the GO nanosheet to other 2D materials such as WS$_2$ and MXene and even carbon nanotube, the metal-containing mesoporous carbon single layer can still be deposited (Fig. 4h, i), holding great promise for various applications.

The development of nonprecious metal catalysts with high activity and outstanding stability for oxygen reduction reaction (ORR) is urgent for large-scale applications of fuel cells[31–33]. Here, the cobalt-containing rGO@mC mesoporous carbon nanosheets annealed at different temperatures (750, 850, and 900 °C) were evaluated for the ORR catalytic activity. Linear sweep voltammetry (LSV) result shows that the sample annealed at 850 °C (rGO@mC-Co-850) exhibits the largest limiting current density (5.97 mA cm^{-2}) and half-wavelength potential (~0.82 V), which is comparable to the commercial platinum–carbon (Pt/C) electrode (Fig. 5a). However, the mass activities of the rGO@mC-Co-850 delivered 2 times larger than that of Pt/C catalyst (Fig. S18). In addition, the performance is better than most previously reported Co-based ORR catalysts (Table S1). The better performance of rGO@mC-Co-850 indicates that the Co species plays an important role in promoting the ORR catalytic activity. Note that the unsmooth limiting current density was possibly due to the continuous bubbling of O$_2$ in the system. The ORR catalytic performance of rGO@mC-Co-850 was then evaluated by cyclic voltammetry (CV) in 0.1 M KOH solution (Fig. 5b). In the N$_2$ saturated solution, a featureless CV curve is observed within the potential ranged from −0.2 to +1.2 V (vs. RHE). When changed to the O$_2$-saturated one, an obvious cathodic peak at 0.76 V appears, which is close to that of the Pt/C electrode (0.77 V).

LSV curves of the rGO@mC-Co-850 were also recorded from 400 to 1600 rpm (Fig. 5c). As the rotation rate rises, the current density is distinctly increased. The relevant Koutecky–Levich (K–L) plots show clear linearity from 0.3 to 0.5 V (Fig. 4D), implying a first-order reaction kinetics for the ORR. Based on the K–L plots, the corresponding electron transfer number (n) of rGO@mC-Co-850 is estimated to be 3.6, suggesting a four-electron transfer pathway[34–36]. After cycling for 5000 cycles, the half-wave potential shows a negligible decrease and the current density can be maintained above 98%, indicating the superior durability of rGO@mC-Co-850 catalyst (Fig. 5e).

To date, the tolerance to the methanol crossover at cathode reactions plays a vital role in the commercialization of fuel cells[37–39]. When a high concentration of methanol (2 mol L^{-1}) was added, an increase of current density and then back to the original was observed in the i–t curve of the rGO@mC-Co-850 electrode (Fig. 5f). The increase of the current density here possibly due to the sudden change of the concentration of reactive species after addition of a massive volume of methanol. As a contrast, the current density was sharply decreased to almost zero for Pt/C catalyst, demonstrating the prominent tolerance to methanol crossover of the rGO@mC-Co-850 catalyst.
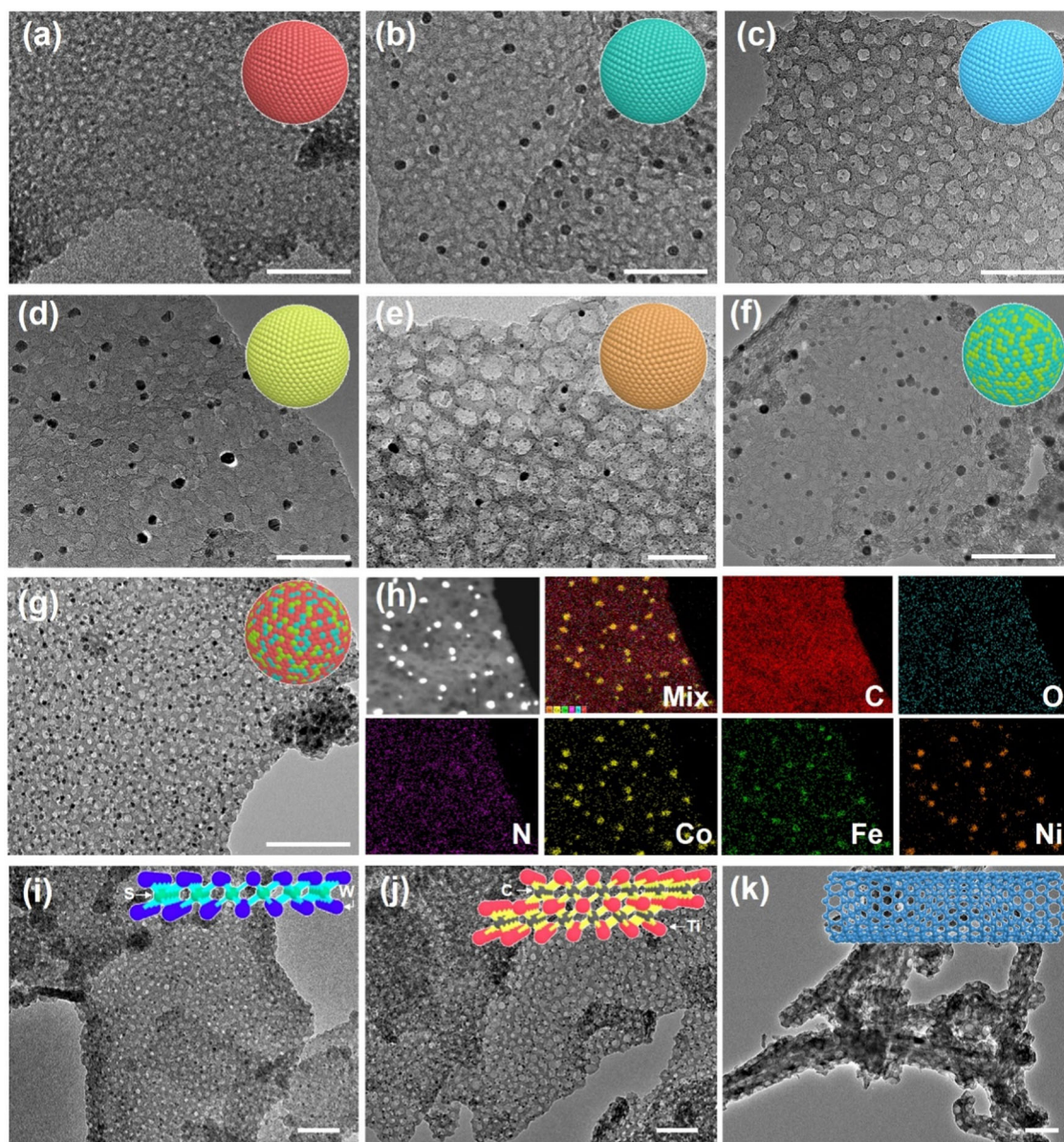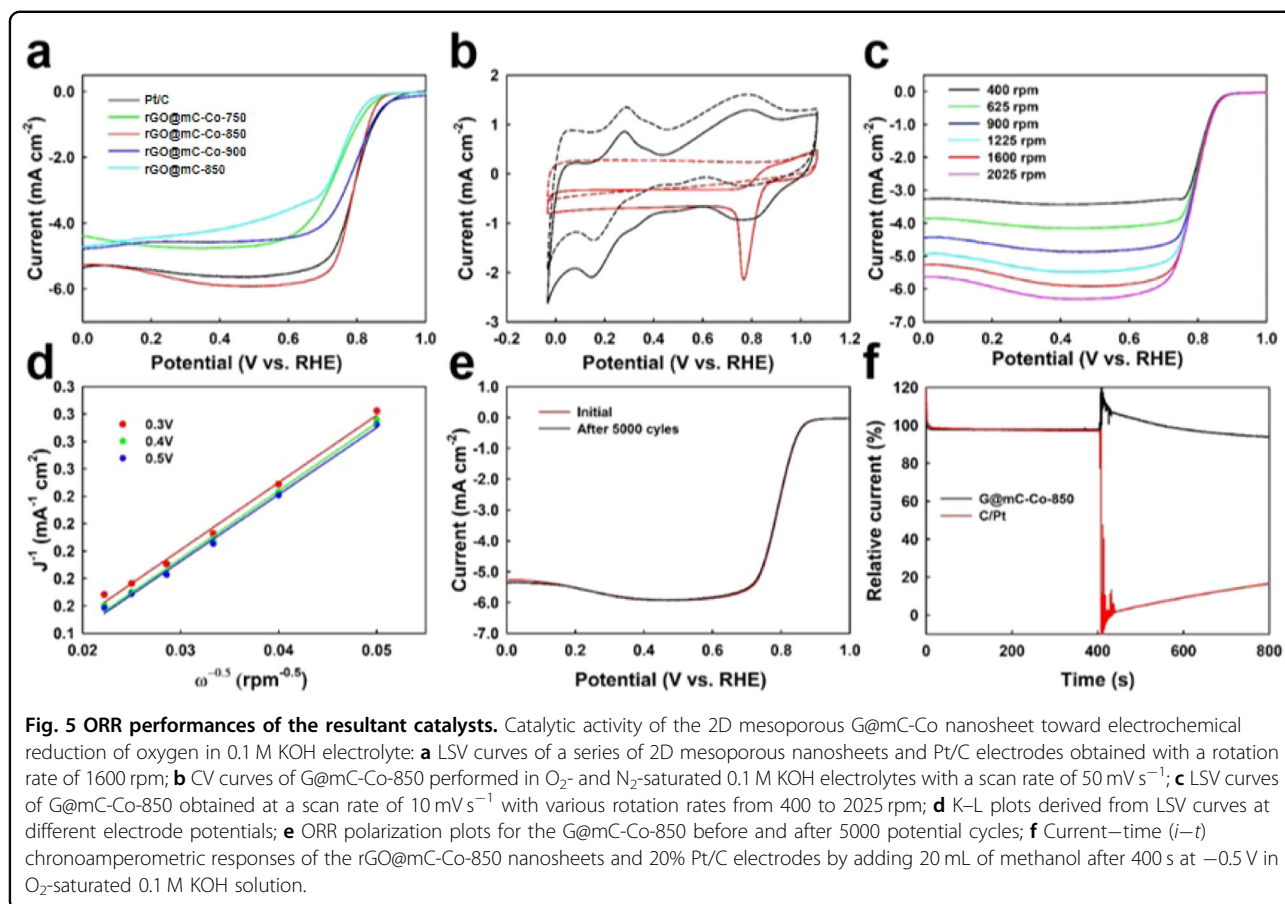
Fig. 4 Charaterization of the extended 2D functional mesoporous materials. TEM images of **a** rGO@mC-V, **b** rGO@mC-Fe, **c** rGO@mC-Ni, **d** rGO@mC-Cu, **e** rGO@mC-Pd, **f** rGO@mC-CoFe, and **g** rGO@mC-CoFeNi. **h** STEM image of rGO@mC-CoFeNi and its corresponding EXS mapping images. TEM images of **i** WS$_2$@mC-Co, **j** Mxene@mC-Co, and **k** CNT@mC-Co. All the scale bars are 100 nm.

The excellent performance of the resultant rGO@mC-Co-850 can be related to its superior textual structures, such as well-defined 2D geometry, ordered mesoporous structure, nitrogen doping, and well-dispersed metal nanoparticles. First, the unique sandwich-like mesoporous structure can provide short pathways for the mass transport of ORR-related species and possess more active sites for catalytic reactions[40–42]. Second, the N-doping in the carbon framework increases electron delocalization due to the good electron-donating property of the N atom, forming abundant active sites for ORR[43–45]. Finally,

the well-dispersed Co nanoparticles in a semi-exposure state may not only provide exposed metal active sites for reactions but also help to tightly trap the nanoparticles and prevent the loss of activity during the reaction applications, which may explain the excellent stability and high methanol tolerance[46–48].

In summary, we have reported a novel interfacial assembly strategy to in-situ construct 2D functional mesoporous carbon nanosheets based on DA/PS-*b*-PEO composite micelle building blocks. The resultant nanosheets possess three layers with a thin 2D nanosheet

Fig. 5 ORR performances of the resultant catalysts. Catalytic activity of the 2D mesoporous G@mC-Co nanosheet toward electrochemical reduction of oxygen in 0.1 M KOH electrolyte: **a** LSV curves of a series of 2D mesoporous nanosheets and Pt/C electrodes obtained with a rotation rate of 1600 rpm; **b** CV curves of G@mC-Co-850 performed in O_2- and N_2-saturated 0.1 M KOH electrolytes with a scan rate of 50 mV s^{-1}; **c** LSV curves of G@mC-Co-850 obtained at a scan rate of 10 mV s^{-1} with various rotation rates from 400 to 2025 rpm; **d** K–L plots derived from LSV curves at different electrode potentials; **e** ORR polarization plots for the G@mC-Co-850 before and after 5000 potential cycles; **f** Current–time ($i-t$) chronoamperometric responses of the rGO@mC-Co-850 nanosheets and 20% Pt/C electrodes by adding 20 mL of methanol after 400 s at −0.5 V in O_2-saturated 0.1 M KOH solution.

(such as graphene, WS_2, and MXene) surrounded by two single-layered mesoporous carbon at both sides, in which the metallic nanoparticles are partially embedded in the pore walls with the remaining part exposed in the mesopore channels. Owing to the high surface area, large pore size, and unique textual structure, the 2D rGO@mC-Co-850 nanosheet exhibited an excellent ORR performance, which is comparable to the commercial C/Pt electrode. More importantly, the catalyst shows high stability (no obvious change of the LSV curve after 5000 cycles) and outstanding methanol tolerance (2 mol L^{-1}), much better than that of the C/Pt electrode. This study holds a promising way for the design and synthesis of 2D functional mesoporous materials for ORR catalysis.

Author contributions
W. Luo, W. Li, and D.Z. conceived the study and corrected the manuscript. P.Q. performed the experiments and wrote the manuscripts. X.Z. and Y.A. analyzed the data. All the authors discussed the results and contributed to data interpretation.

Conflict of interest
The authors declare no competing interests.

Publisher's note
Springer Nature remains neutral with regard to jurisdictional claims in published maps and institutional affiliations.

Supplementary information The online version contains supplementary material available at https://doi.org/10.1038/s41427-023-00482-z.

References
1. Mao, L.-B. et al. Synthetic nacre by predesigned matrix-directed mineralization. *Science* **354**, 107–110 (2016).
2. Zheng, J. et al. From molecular to macroscopic via the rational design of a self-assembled 3D DNA crystal. *Nature* **461**, 74–77 (2009).
3. Coleman, A. C. et al. Light-induced disassembly of self-assembled vesicle-capped nanotubes observed in real time. *Nat. Nanotechnol.* **6**, 547–552 (2011).
4. Ma, K. et al. Self-assembly of highly symmetrical, ultrasmall inorganic cages directed by surfactant micelles. *Nature* **558**, 577–580 (2018).
5. Ren, Y. et al. Synthesis of orthogonally assembled 3D cross-stacked metal oxide semiconducting nanowires. *Nat. Mater.* **19**, 203–211 (2020).

6. Shi, S. & Russell, T. P. Nanoparticle assembly at liquid–liquid interfaces: from the nanoscale to mesoscale. *Adv. Mater.* **30**, 1800714 (2018).

7. Duan, L. et al. Synthesis of fully exposed single-atom-layer metal clusters on 2D ordered mesoporous TiO_2 nanosheets. *Angew. Chem. Int. Ed.* **61**, e202211307 (2022).

8. Hung, C.-T. et al. Gradient hierarchically porous structure for rapid capillary-assisted catalysis. *J. Am. Chem. Soc.* **144**, 6091–6099 (2022).

9. Zhao, Z. et al. General synthesis of ultrafine monodispersed hybrid nanoparticles from highly stable monomicelles. *Adv. Mater.* **33**, 2100820 (2021).

10. Qiu, P., Ma, B., Hung, C.-T., Li, W. & Zhao, D. Spherical mesoporous materials from single to multilevel architectures. *Acc. Chem. Res.* **52**, 2928–2938 (2019).

11. Li, W., Elzatahry, A., Aldhayan, D. & Zhao, D. Core–shell structured titanium dioxide nanomaterials for solar energy utilization. *Chem. Soc. Rev.* **47**, 8203–8237 (2018).

12. Liu, L. et al. A universal lab-on-salt-particle approach to 2D single-Layer ordered mesoporous materials. *Adv. Mater.* **32**, 1906653 (2020).

13. Wang, J. et al. Universal access to two-dimensional mesoporous heterostructures by micelle-directed interfacial assembly. *Angew. Chem. Int. Ed.* **132**, 19738–19743 (2020).

14. Qin, J. et al. Hierarchical ordered dual-mesoporous polypyrrole/graphene nanosheets as bi-functional active materials for high-performance planar integrated system of micro-supercapacitor and gas sensor. *Adv. Funct. Mater.* **30**, 1909756 (2020).

15. Qiu, P. et al. Sub-nanometric manganous oxide clusters in nitrogen doped mesoporous carbon nanosheets for high-performance lithium–sulfur batteries. *Nano Lett.* **21**, 700–708 (2020).

16. Zhu, G. et al. Constructing structurally ordered high-entropy alloy nanoparticles on nitrogen-rich mesoporous carbon nanosheets for high-performance oxygen reduction. *Adv. Mater.* **34**, 2110128 (2022).

17. Lan, K. et al. Two-dimensional mesoporous heterostructure delivering superior pseudocapacitive sodium storage via bottom-up monomicelle assembly. *J. Am. Chem. Soc.* **141**, 16755–16762 (2019).

18. Guo, J. et al. Modular assembly of superstructures from polyphenol-functionalized building blocks. *Nat. Nanotechnol.* **11**, 1105–1111 (2016).

19. Rahim, M. A., Kristufek, S. L., Pan, S., Richardson, J. J. & Caruso, F. Phenolic building blocks for the assembly of functional materials. *Angew. Chem. Int. Ed.* **58**, 1904–1927 (2019).

20. Zhou, J. et al. Polyphenol-mediated assembly for particle engineering. *Acc. Chem. Res.* **53**, 1269–1278 (2020).

21. Liu, S. et al. Patterning two-dimensional free-standing surfaces with mesoporous conducting polymers. *Nat. Commun.* **6**, 8817 (2015).

22. Liu, S. et al. Dual-template synthesis of 2D mesoporous polypyrrole nanosheets with controlled pore size. *Adv. Mater.* **28**, 8365–8370 (2016).

23. Cho, J., Hong, J., Char, K. & Caruso, F. Nanoporous block copolymer micelle/micelle multilayer films with dual optical properties. *J. Am. Chem. Soc.* **128**, 9935–9942 (2006).

24. Holten-Andersen, N. et al. pH-induced metal–ligand cross-links inspired by mussel yield self-healing polymer networks with near-covalent elastic moduli. *Proc. Natl Acad. Sci. USA* **108**, 2651–2655 (2011).

25. Liu, R. et al. An interface-induced co-assembly approach towards ordered mesoporous carbon/graphene aerogel for high-performance supercapacitors. *Adv. Funct. Mater.* **25**, 526–533 (2015).

26. Song, R. et al. Ultrafine nanoporous intermetallic catalysts by high-temperature liquid metal dealloying for electrochemical hydrogen production. *Nat. Commun.* **13**, 5157 (2022).

27. Yu, P. et al. Co nanoislands rooted on Co–N–C nanosheets as efficient oxygen electrocatalyst for Zn–air batteries. *Adv. Mater.* **31**, 1901666 (2019).

28. Zhu, G. et al. Modulating the electronic structure of FeCo nanoparticles in N-doped mesoporous carbon for efficient oxygen reduction reaction. *Adv. Sci.* **9**, 2200394 (2022).

29. Singh, S. K., Takeyasu, K. & Nakamura, J. Active sites and mechanism of oxygen reduction reaction electrocatalysis on nitrogen-doped carbon materials. *Adv. Mater.* **31**, 1804297 (2019).

30. Fernandez-Escamilla, H. N. et al. Understanding the selectivity of the oxygen reduction reaction at the atomistic level on nitrogen-doped graphitic carbon materials. *Adv. Energy Mater.* **11**, 2002459 (2021).

31. Gewirth, A. A., Varnell, J. A. & DiAscro, A. M. Nonprecious metal catalysts for oxygen reduction in heterogeneous aqueous systems. *Chem. Rev.* **118**, 2313–2339 (2018).

32. Liu, J. et al. Hydrogen passivation of M–N–C (M = Fe, Co) catalysts for storage stability and ORR activity improvements. *Adv. Mater.* **33**, 2103600 (2021).

33. Al-Zoubi, T. et al. Preparation of nonprecious metal electrocatalysts for the reduction of oxygen using a low-temperature sacrificial metal. *J. Am. Chem. Soc.* **142**, 5477–5481 (2020).

34. Liang, Z. et al. Metal-organic-framework-supported molecular electrocatalysis for the oxygen reduction reaction. *Angew. Chem. Int. Ed.* **133**, 8553–8557 (2021).

35. Yang, J. et al. Compressive strain modulation of single iron sites on helical carbon support boosts electrocatalytic oxygen reduction. *Angew. Chem. Int. Ed.* **60**, 22722–22728 (2021).

36. Tong, M. et al. Operando cooperated catalytic mechanism of atomically dispersed $Cu-N_4$ and $Zn-N_4$ for promoting oxygen reduction reaction. *Angew. Chem. Int. Ed.* **60**, 14005–14012 (2021).

37. Ma, M. et al. Diluted silicon promoting Pd/Pt catalysts for oxygen reduction reaction with strong anti-poisoning effect. *Appl. Catal. B: Environ.* **315**, 121549 (2022).

38. Liu, X. et al. A stable bifunctional catalyst for rechargeable zinc–air batteries: iron–cobalt nanoparticles embedded in a nitrogen-doped 3D carbon matrix. *Angew. Chem. Int. Ed.* **57**, 16166 (2018).

39. Xing, G. et al. Reconstruction of highly dense $Cu-N_4$ active sites in electrocatalytic oxygen reduction characterized by operando synchrotron radiation. *Angew. Chem. Int. Ed.* **61**, e202211098 (2022).

40. Peng, L. et al. Versatile nanoemulsion assembly approach to synthesize functional mesoporous carbon nanospheres with tunable pore sizes and architectures. *J. Am. Chem. Soc.* **141**, 7073–7080 (2019).

41. Ai, Y., Li, W. & Zhao, D. Y. 2D mesoporous materials. *Natl Sci. Rev.* **9**, nwab108 (2022).

42. Li, C., Li, Q., Kaneti, Y., Yamauchi, Y. & Mai, Y. Y. Self-assembly of block copolymers towards mesoporous materials for energy storage and conversion systems. *Chem. Soc. Rev.* **49**, 4681–4736 (2020).

43. Guo, D. et al. Active sites of nitrogen-doped carbon materials for oxygen reduction reaction clarified using model catalysts. *Science* **351**, 361–365 (2016).

44. Singh, S. K., Takeyasu, K. & Nakamura, J. Active sites and mechanism of oxygen reduction reaction electrocatalysis on nitrogen-doped carbon materials. *Adv. Mater.* **31**, 1804297 (2019).

45. Jiang, H. et al. Defect-rich and ultrathin N doped carbon nanosheets as advanced trifunctional metal-free electrocatalysts for the ORR, OER and HER. *Energy Environ. Sci.* **12**, 322–333 (2019).

46. Yang, C. C., Zai, S. F., Zhou, Y. T., Du, L. & Jiang, Q. Fe_3C-Co nanoparticles encapsulated in a hierarchical structure of N-Doped carbon as a multifunctional electrocatalyst for ORR, OER, and HER. *Adv. Funct. Mater.* **29**, 1901949 (2019).

47. Wang, T. et al. Sub-6 nm fully ordered L_{10}-Pt–Ni–Co nanoparticles enhance oxygen reduction via Co doping induced ferromagnetism enhancement and optimized surface strain. *Adv. Energy Mater.* **9**, 1803771 (2019).

48. Kim, C. et al. Alloy nanocatalysts for the electrochemical oxygen reduction (ORR) and the direct electrochemical carbon dioxide reduction reaction (CO_2RR). *Adv. Mater.* **31**, 1805617 (2019).